High-Performance Aqueous Supercapacitors Based on a Self-Doped n-Type Conducting Polymer

Ohayon, David; Quek, Glenn; Yip, Benjamin Rui Peng; Lopez-Garcia, Fernando; Ng, Pei Rou; Vázquez, Ricardo Javier; Andreeva, Daria V.; Wang, Xuehang; Bazan, Guillermo C.

DOI
10.1002/adma.202410512

Publication date
2024

Document Version
Final published version

Published in
Advanced Materials

Citation (APA)
Ohayon, D., Quek, G., Yip, B. R. P., Lopez-Garcia, F., Ng, P. R., Vázquez, R. J., Andreeva, D. V., Wang, X., & Bazan, G. C. (2024). High-Performance Aqueous Supercapacitors Based on a Self-Doped n-Type Conducting Polymer. *Advanced Materials*, *36*(47), Article 2410512. https://doi.org/10.1002/adma.202410512

ADVANCED MATERIALS
www.advmat.de

High-Performance Aqueous Supercapacitors Based on a Self-Doped n-Type Conducting Polymer

David Ohayon, Glenn Quek, Benjamin Rui Peng Yip, Fernando Lopez-Garcia, Pei Rou Ng, Ricardo Javier Vázquez, Daria V. Andreeva, Xuehang Wang, and Guillermo C. Bazan**

Environmentally-benign materials play a pivotal role in advancing the scalability of energy storage devices. In particular, conjugated polymers constitute a potentially greener alternative to inorganic- and carbon-based materials. One challenge to wider implementation is the scarcity of n-doped conducting polymers to achieve full cells with high-rate performance. Herein, this work demonstrates the use of a self-doped n-doped conjugated polymer, namely poly(benzodifurandione) (PBDF), for fabricating aqueous supercapacitors. PBDF demonstrates a specific capacitance of 202 ± 3 F g^{-1}, retaining 81% of the initial performance over 5000 cycles at 10 A g^{-1} in 2 M $NaCl_{(aq)}$. PBDF demonstrates rate performances of up to 100 and 50 A g^{-1} at 1 and 2 mg cm^{-2}, respectively. Electrochemical impedance analysis reveals a surface-mediated charge storage mechanism. Improvements can be achieved by adding reduced graphene oxide (rGO), thereby obtaining a specific capacitance of 288 ± 8 F g^{-1} and high-rate operation (270 A g^{-1}). The performance of PBDF is examined in symmetric and asymmetric membrane-less cells, demonstrating high-rate performance, while retaining 83% of the initial capacitance after 100 000 cycles at 10 A g^{-1}. PBDF thus offers new prospects for energy storage applications, showcasing both desirable performance and stability without the need for additives or binders and relying on environmentally friendly solutions.

1. Introduction

Sustainable and efficient energy storage continues to be a driving force in materials science innovation and electrochemical engineering. Three key areas are of particular relevance: wearable electronics —requiring power sources of flexible shapes and forms with low but fast and stable charge, electric mobility —calling for high power and high energy sources for long-range driving, and low cost and stationary long life storage devices for balancing the electricity grid.[1] Batteries store charges through Faradaic processes and constitute the most widely used platform for energy storage, with the Li-ion battery technology as their gold standard. While this storage mechanism grants batteries high energy densities, it is also one of their biggest tradeoffs, endowing batteries with comparatively slow charging and discharging rates, therefore restricting the achievable power density. Supercapacitors, on the other hand, are characterized by their high power density and extended cycling life (>1 million cycles) through surface-controlled charge storage processes.[2] However, the ever-growing demand for energy storage places important pressure on the supply of lithium (batteries) and transition metals (supercapacitors) that are used as electrode materials.[3,4] Both types of devices also often rely on corrosive and/or flammable electrolytes, and thus present safety and environmental concerns, while their aqueous-based alternatives remain commercially underdeveloped. As our society moves toward electromobility and decarbonization of its energy supply, there is an obvious need for developing energy storage devices that provide compromising performance metrics, such as intermediate power and energy densities, fast charging capabilities, and long cyclability, in combination with increased safety and minimal environmental footprint.

Within the context of the preceding background, electrochemical pseudocapacitors provide an alternative, presenting performances mid-way between capacitors and batteries thanks to near-surface redox reaction or pseudocapacitive counter ion.[5] As such, conjugated polymer-based pseudocapacitors have emerged as promising candidates for sustainable energy storage, as they comprise earth-abundant carbon, oxygen, hydrogen, and nitrogen.[4,6–8] Indeed, conjugated polymers present characteristic features that set them apart from other materials.[9,10] They

D. Ohayon, F. Lopez-Garcia, P. R. Ng, R. J. Vázquez, D. V. Andreeva, G. C. Bazan
Institute for Functional Intelligent Materials
National University of Singapore
Singapore 117544, Singapore
E-mail: chmbgc@nus.edu.sg
D. Ohayon, G. Quek, B. R. P. Yip, F. Lopez-Garcia, R. J. Vázquez, G. C. Bazan
Departments of Chemistry and Chemical & Biomolecular Engineering
National University of Singapore
Singapore 119077, Singapore
P. R. Ng, D. V. Andreeva
Department of Materials Science and Engineering
National University of Singapore
Singapore 117575, Singapore
R. J. Vázquez
Department of Chemistry
Indiana University
Bloomington, Indiana 47405, USA
X. Wang
Department of Radiation Science and Technology
Delft University of Technology
Delft 2629 JB, The Netherlands
E-mail: x.wang-22@tudelft.nl
The ORCID identification number(s) for the author(s) of this article can be found under https://doi.org/10.1002/adma.202410512

DOI: 10.1002/adma.202410512

can be processed from solution at room temperature, potentially enabling low-cost and scalable manufacturing, while other inorganic/carbon materials may require high sintering temperatures and more complex fabrication processes. Moreover, conjugated polymers can be designed to enable transport of both electronic and ionic charges throughout their bulk, where these mixed conduction properties, together with their inherent softness and tunable mechanical properties, open opportunities for fabricating devices with flexible form factors. Last but not least, their versatile chemistry allows for a fine-tuning of their electronic properties, in particular, the design of hole (p-type) and/or electron (n-type) transporting materials.[7]

Despite these compelling properties, conjugated polymer-based supercapacitors are not yet technologically competitive, mainly due to generally lower conductivity and cycling stability compared to carbon-based counterparts, thus requiring additives or post-processing steps to improve properties relevant to cell performance.[6,11,12] Another limitation lies in the restricted library of available n-type materials for supercapacitor electrodes, thereby restricting all-polymeric supercapacitors to predominantly p-type symmetric cell configurations with limited performance due to narrow voltage windows.[10] Alternative asymmetric cells pairing a p-type polymer with a carbon electrode are hampered by the double-layer dominated carbon electrode.[10] Therefore, an asymmetric all-polymeric supercapacitor would benefit from an optimized voltage window and high redox-based capacitance. The few viable n-type polymers display generally lower conductivity and more instability than their p-type counterparts, typically because of their sensitivity toward oxygen and water.[13–15] It is worth highlighting the seminal work on perylenediimide contorted electrodes and subsequent iterations representing the current state-of-the-art performances for n-based electrodes.[16–18] However, these examples typically require the use of carbon additives and binders to operate, thereby increasing fabrication complexity. In contrast, there are only a few all-polymeric supercapacitors reported, most leveraging different p-type polymers, while the poly(benzimidazobenzophenantroline) -BBL-based supercapacitor of Volkov et al. remains a noteworthy competitive asymmetric example.[19–22] Furthermore, among the very few n-type polymers used in energy storage applications, there is an absence of n-type polymers that can deliver high-rate performance. Overall, high-performance n-type conjugated polymers for electrochemical supercapacitors remain a challenge that must be overcome to achieve further improvements in all-conjugated polymer pseudocapacitors.

Herein, we report the pseudocapacitive performance of the n-type conjugated polymer poly(benzodifurandione) (PBDF).[23] We show that PBDF, which was first synthesized in Huang's group, can be processed using environmentally friendly dimethyl sulfoxide solution for the fabrication of aqueous supercapacitors.[24] PBDF demonstrates a high specific capacitance of 202 ± 3 F g^{-1}, high rate capabilities (200 A g^{-1}), and good cycling stability. Electrochemical impedance spectroscopy analysis (EIS) reveals characteristics associated with surface-mediated storage mechanisms. We also examined the performance of PBDF in more practical configurations, both in symmetric and asymmetric membrane-less cells. The resulting devices are among the best-performing polymer-based supercapacitors with relatively high power (10^4–10^5 W kg^{-1}) and energy (≈10 Wh kg^{-1}) densities, while presenting the advantage of single-component composition. Further improvements in PBDF performance can be achieved by adding reduced graphene oxide (rGO) to increase the polymer utilization rate. The PBDF:rGO blend achieves a specific capacitance of 288 ± 8 F g^{-1} and high-rate operation, as high as 270 A g^{-1}. When implemented in symmetric and asymmetric cells, PBDF:rGO maintained its high-rate operation, while demonstrating excellent cyclability, retaining 83% of its capacitance after 100 000 cycles at 10 A g^{-1}. Moreover, PBDF was shown to maintain its good rate capabilities (up to 100 and 50 A g^{-1} at 1 and 2 mg cm^{-2}, respectively) and high stability (>90% after 5000 cycles) at mass loadings meaningful for practical applications, an unprecedented feat for a single-system n-type conjugated polymer. Overall, the excellent performance and stability of PBDF are of important scientific significance and argue in favor of the practical use of polymeric-based energy storage technology.

2. Results and Discussion

PBDF was synthesized following literature precedent (see Methods section and **Figure 1a** for the chemical structure).[24] The resulting PBDF was then purified by dialysis to yield a PBDF solution in DMSO with an initial concentration of 1.83 mg mL^{-1}. The solution of PBDF in DMSO was drop cast (5 µL) on a polished glassy carbon electrode (GCE; ø = 3.0 mm) and left to dry in a vacuum oven at 60 °C for at least 4 h. Scanning electron microscopy (SEM) images reveal a smooth surface with small cracks (Figure S1, Supporting Information), similar to previous reports.[24] The resulting film is conductive, as measured by 4-point probe, with a conductivity of 321 ± 123 S cm^{-1} (Figure S2a, Supporting Information). The relatively large error in the conductivity estimation stems from the uncertainty in the thickness estimation (1.04 ± 0.32 µm), mainly due to high roughness. Electron paramagnetic resonance spectroscopy (EPR) reveals an unpaired signal in PBDF, in line with the self-doped state and high conductivity of the film (Figure S2b, Supporting Information).[24]

To assess the feasibility of using PBDF for electrochemical supercapacitor applications, we first examined the redox behavior and kinetics of PBDF by using a three-electrode cell. Figure 1a shows the cyclic voltammogram (CV) of a PBDF film in 2 M $NaCl_{(aq)}$, which exhibited a reduction onset at ≈0.41 V, in line with previous reports.[24,25] We further note a capacitive envelope in the negative potential region (from 0 to −0.8 V), foreshadowing the potential of PBDF as an n-type conducting polymer for energy storage applications. CV measurements were also carried out at different scan rates (from 5 to 500 mV s^{-1}, see Figure S3a, Supporting Information) and the resulting traces were analyzed according to the power law $i_p = a\nu^b$, where the b value describes the reaction-diffusion behavior.[26] Generally, a b value of 0.5 is characteristic of an ion diffusion-controlled process. In contrast, a value of 1.0 suggests a surface-controlled electrochemical process.[27] The log(i_p)-log(ν) plot reveals a b value of 0.9 up to 500 mV s^{-1}, in line with a surface-controlled charge storage mechanism (Figure S3b, Supporting Information). Moreover, the method developed by Trasatti et al. on the relationship between the capacity Q and scan rate provides further insights.[28,29] A plot of $1/Q$ as a function of $\nu^{1/2}$ exhibits a linear dependence for the

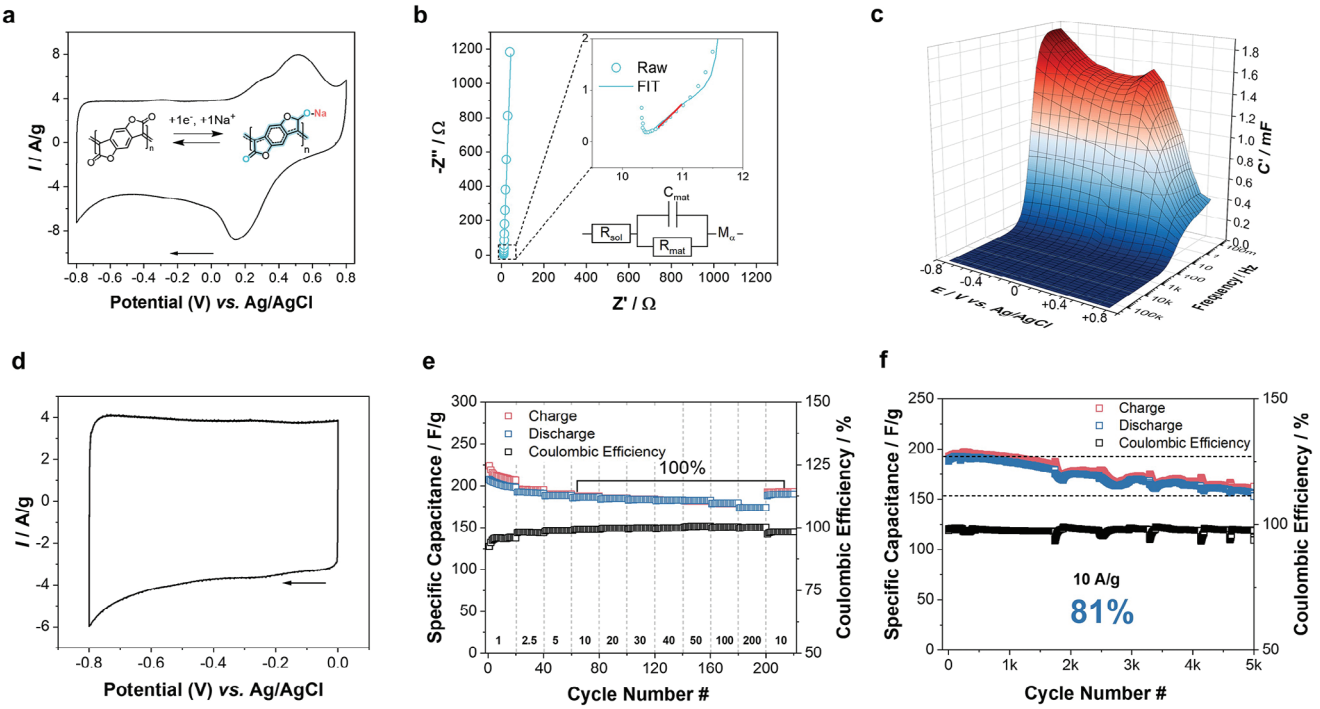

Figure 1. Electrochemical characterization of PBDF for energy storage. a) CV curve of PBDF thin film drop casted atop a glassy carbon electrode and chemical structure of PBDF. The scan rate is 20 mV s^{-1} and the arrow indicates the scan direction. Schematic of the suggested electrochemical charge storage mechanism of PBDF via a 1 electron reduction. b) Nyquist plot of PBDF at open-circuit potential (0.124 V versus Ag/AgCl) from 100 kHz to 0.1 Hz shows a small 45° slope (red line) followed by a near 90° slope, characteristic of a restricted linear diffusion (inset). The equivalent electronic circuit is shown with the corresponding fit. c) Real Capacitance *C'* as a function of frequency and potential. d) CV of a PBDF electrode for electrochemical supercapacitor characterization. Scan rate is 20 mV s^{-1} and the arrow indicates the scan direction. e) Rate performance of PBDF obtained from Galvanostatic charge-discharge (GCD). The specific capacitance (charge in red and discharge in blue, left axis) and Coulombic efficiency (black, right axis) are represented for each current density (A g^{-1}). Each current density is applied for 20 cycles. Dotted lines demark each current density and their corresponding value is indicated above the x-axis. f) Cycling stability (from GCD) over 5000 cycles at a current density of 10 A g^{-1}. The left axis displays the specific capacitance (charge in red and discharge in blue), and the right axis the coulombic efficiency (black).

scan rate range investigated here, from which the extrapolation to $\nu = 0$ mV s^{-1} estimates the total accessible charge of PBDF (Q_{tot}). Alternatively, the extrapolation of Q versus $\nu^{-1/2}$ to $\nu = \infty$ provides an estimation of the capacity at an infinite sweep rate, that is, the outer charge of the material (Q_{outer}). We find Q_{outer} = 611 C g^{-1}, representing 66% of the total charge Q_{tot} = 926 C g^{-1} (Figure S4, Supporting Information), confirming a kinetic behavior similar to surface-dominated charge storage mechanisms. Furthermore, extracting the number of electrons from the cathodic and anodic capacity at the different scan rates reveals ≈0.7–0.9 electrons per structural repeating unit, echoing previously reported results (Table S1, Supporting Information).[24]

The redox kinetics of the PBDF films were examined. Applying the Randles–Ševčík equation (see Equations (S1) and (S2), Supporting Information in Methods) yields an apparent diffusion coefficient D_{app} = 5.38 × 10^{-12} cm^2 s^{-1}, in the range of other redox-active and conjugated polymers.[30,31] We calculated the self-exchange reaction rate constant k_{ex} using the Dahms-Ruff model and found k_{ex} = 1.11 × 10^6 $M^{-1}s^{-1}$, within the same range of the calculated k_{ex} = 3.96 × 10^5 $M^{-1}s^{-1}$ for BBL, one of the only few n-type conjugated polymers studied in the context of energy storage.[30] These values translate into fast charge transport kinetics, essential for high performance. Insights into the electronic and ionic resistances of the system were obtained by recording the EIS spectra of PBDF under different biases (from +0.8 to −0.8 V). The Nyquist impedance does not exhibit any observable semi-circle, while a short 45° slope at mid-high frequencies (red line) transitioning into a near 90° slope at mid-low frequencies is observed. These observations are in agreement with the expected surface-controlled charge storage mechanism of supercapacitors where most of the reactive sites are easily accessible within a short period of time (Figure 1b, inset).[27,32] We used a modified Randles circuit to fit the impedance spectra, replacing the traditional Warburg element with a restricted modified linear diffusion element M_a, more representative of the diffusion slope transition observed (Figure 1b, Table S2, Supporting Information).[33] An excellent fit is achieved (χ^2 = 2.33 × 10^{-3}), from which the M_a impedance equation (Equation 1) enables the extraction of relevant diffusion-related parameters, namely the diffusion resistance (R_D) and diffusion time constant (τ_D) —representing how hard and fast a solute can diffuse, according to:

$$Z_{M_a}(f) = R_D \frac{\coth(\tau_D j 2\pi f)^{\alpha/2}}{(\tau_D j 2\pi f)^{\alpha/2}} \quad (1)$$

where j is $(-1)^{-1/2}$, f is the frequency, τ_D is the diffusion time constant and R_D is the diffusional resistance, and α is a dispersion

parameter.[34] Further, τ_D is directly related to the ion diffusion coefficient D_{ion} and thickness of the electrode (δ), according to:[33]

$$\tau_D = \frac{\delta^2}{D_{ion}} \quad (2)$$

Through this analysis, we determined that $R_D = 3.33 \pm 0.14$ Ω and $\tau_D = 4.29 \pm 0.19$ ms, yielding an ion diffusion coefficient $D_{ion} = 2.53 \times 10^{-6}$ cm^2 s^{-1}, demonstrating overall rapid ion diffusion and comparable ionic transport to conjugated polyelectrolytes and PEDOT:PSS.[35,36]

We aimed to build a more complete description and understanding of the capacitive storage mechanism of PBDF using a 3D-Bode plot analysis (Figures 1c and S5, Supporting Information). This analysis visualizes the frequency- and potential-dependent capacitance and phase impedance, where the possible superposition of multiple charge-storage processes (i.e., double layer, pseudocapacitive, or faradaic) becomes more evident.[37–39] The 3D representation of the real part of the capacitance *C'* and phase angle as a function of potential and frequency reveals a complex charge storage mechanism over the potential range investigated (Figures 1c and S5, Supporting Information). From −0.8 to +0.3 V, *C'* displays a "waterfall" shape, slightly decreasing from −0.8 V with more positive potentials and falling off as frequency increases, while the phase angle is relatively constant at −88°, both characteristic of a capacitive charge storage mechanism.[37] From +0.3 to +0.8 V, however, that is, when PBDF reverts to its neutral state, both *C'* and the phase angle decrease sharply with potential while preserving the same frequency-dependence, exemplary of a pseudocapacitive mechanism.[37] These results are further supported by in situ conductivity measurements, where PBDF demonstrates a constant conductivity from −0.8 V up to +0.3 V, after which the conductivity drops (Figure S6, Supporting Information). Taken all together, these results support a rapid surface-dominated charge storage mechanism within the negative potential region.

We probed the charge storage performance of PBDF in a three-electrode configuration. From the previous EIS analysis, PBDF demonstrates a capacitive charge storage mechanism in the negative potential region (from 0 to −0.8 V), while its capacitance falls off when approaching its redox couple region. Moreover, PBDF was previously shown to display cycling instability when poised near its neutral state.[24] Therefore, we selected a potential window from 0 to −0.8 V to evaluate the charge storage performance of PBDF. This potential window displays a rectangular box-like CV trace (Figure 1d) and was used in galvanostatic charge-discharge (GCD) cycles to evaluate the rate performance. Of note is that we tested 2 M $NaCl_{(aq)}$, 2 M $KCl_{(aq)}$, and 1 M $Na_2SO_{4(aq)}$ (Figure S7, Supporting Information). Out of the different electrolytes, PBDF displays the best performances in $NaCl_{(aq)}$ – a previously observed phenomenon attributed to the lower ionic radius of Na^+ and Cl^- compared to K^+ and SO_4^{2-}, respectively, and consequently, higher ionic mobility.[40] Therefore, unless stated otherwise, all subsequent measurements were performed in 2 M $NaCl_{(aq)}$.

PBDF displays triangular GCD traces with minimal IR drop, even at 200 A g^{-1} (Figure S8, Supporting Information), and demonstrates excellent rate performance up to 200 A g^{-1}, yielding a specific capacitance of 202 ± 3 F g^{-1} at 1 A g^{-1} and 174 ± 1 F g^{-1} at 200 A g^{-1}, thereby maintaining 86% of its capacitance at high operation rate (Figure 1e). Further, PBDF displays good operation reversibility by retaining ≈100% of its specific capacitance at 10 A g^{-1} after more than 200 cycles at increasing current densities (Figure 1e), and exhibits good cycling stability, retaining 81% of its initial capacitance after 5000 cycles at 10 A g^{-1} (Figure 1f). Overall, PBDF demonstrates promising specific capacitance and reversible operation, both under variable and constant load, outperforming numerous recently reported state-of-the-art n-type organic materials.[13,17,19,41–44] Other caveats of PBDF compared to other reported materials: the performances presented here are from a single component system in the absence of additives or binders.[16,41] Furthermore, many reports employ corrosive aqueous electrolytes (e.g., 6 M KOH or 1 M H_2SO_4), while PBDF displays excellent performance in neutral $NaCl_{(aq)}$, unlocking more straightforward device fabrication and safer applications. We summarize the performance metrics for PBDF (along with PBDF blends, see below) measured in a 3-electrodes cell configuration in **Table 1**.

Table 1. Electrochemical performance of PBDF-based electrodes measured in a three-electrode configuration in degassed 2 M $NaCl_{(aq)}$.

	Voltage window	Specific Capacitance	Rate Capability
	[V]	[F g^{-1}]	[%Specific Capacitance]
PBDF	0.8	202 ± 3	86% at 200 A g^{-1}
PBDF:GO (2:1)	0.8	225 ± 2	81% at 270 A g^{-1}
PBDF:GO (5:1)	0.8	262 ± 3	75% at 270 A g^{-1}
PBDF:rGO (2:1)	0.8	288 ± 8	77% at 270 A g^{-1}
PBDF:rGO (5:1)	0.8	223 ± 5	83% at 270 A g^{-1}

We sought to understand the charge storage and cycling effects on the PBDF chemical structure. Spectroelectrochemistry measurements highlight the change in optical absorption as a function of PBDF doping levels (Figure S9, Supporting Information). The spectra of the pristine PBDF exhibit a broad absorption peak centered ≈500 nm. Application of a doping potential leads to the decrease in intensity of the band at 500 nm, concomitant with the appearance of a new feature centered ≈400 nm. The changes in optical absorption of PBDF with increasing doping potential suggest that in its pristine state, PBDF is not fully doped. FTIR spectroscopy was used to probe possible changes in chemical structure as a result of charging–discharging cycles (**Figure 2a** and Table S3, Supporting Information). Upon charging PBDF, the hetero-ring C—O—C (1190 and 1278 cm^{-1}) and C=C (1464 cm^{-1}) vibrations shift toward higher wavenumbers. The C=O (1774 cm^{-1}) vibration shifts toward lower wavenumbers (Table S3, Supporting Information), suggesting the complexation between the carbonyl group and Na^+.[45] Further, we note a decrease in intensity and broadening of the C=C and C=O peaks in the charged sample (Figure 2a, red), which recovers after returning to the discharged state (Figure 2a, blue). Last, the FTIR spectrum of PBDF after 1000 GCD cycles does not exhibit any significant changes compared to the pristine sample, suggesting that PBDF is able to maintain its molecular integrity through cycling, echoing the capacitance retention demonstrated above in Figure 1e,f.

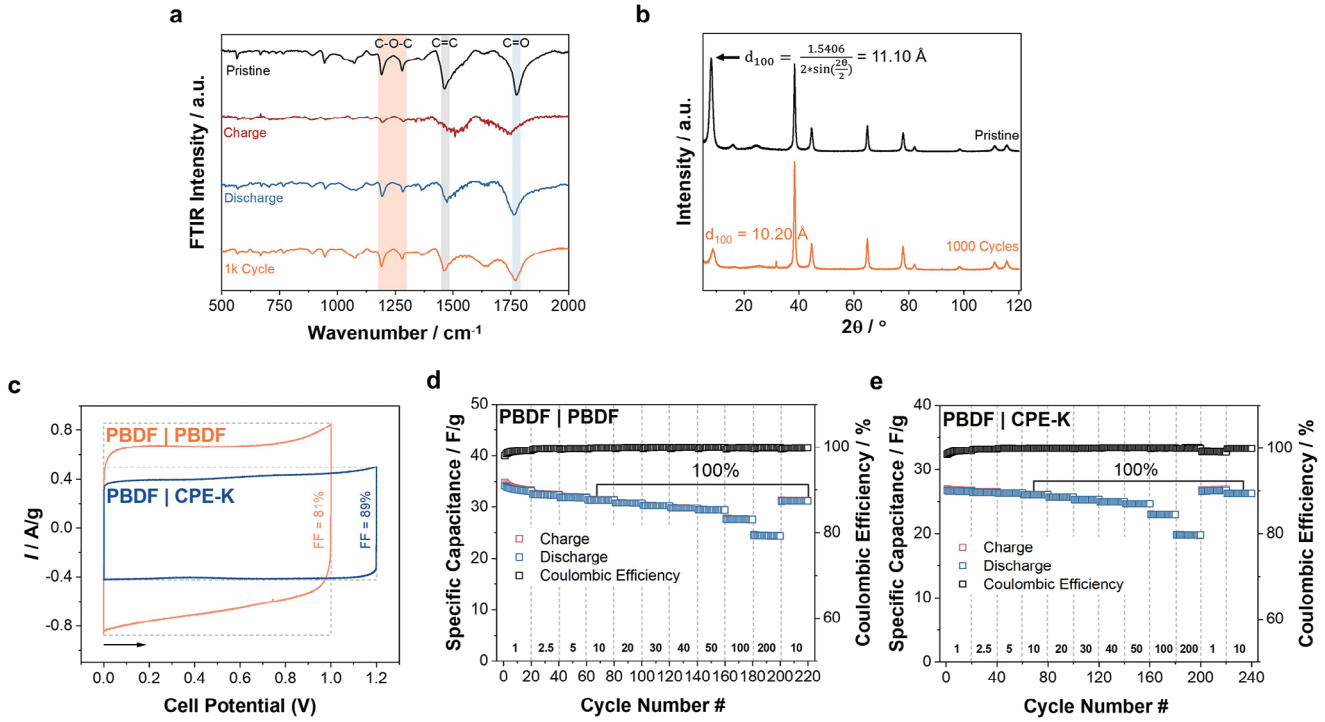

Figure 2. Electrochemical charge storage mechanism of PBDF. a) ATR-FTIR spectra of the pristine (black), charged (red), discharged (blue), and cycled 1000 times at 10 A g^{-1} (orange) PBDF films. The hetero-ring C—O—C (orange), C=C (grey), and C=O (blue) characteristic stretching vibrations are highlighted. b) XRD peak patterns of the pristine (black) and after 1000 GCD cycles at 10 A g^{-1} (presented in its discharged state, orange) PBDF films. The calculated distance for the d_{100} peak (at ≈7.96°) is shown for each sample. c) CV curves of the PBDF|PBDF (orange) and PBDF|CPE-K (blue) supercapacitors in 2 M $NaCl_{(aq)}$. Scan rate is 20 mV s^{-1} and arrow indicates the scan direction, FF = fill factor. d,e) Rate performance of symmetric PBDF|PBDF (d) and asymmetric PBDF|CPE-K (e) supercapacitors. The specific capacitance (charge in red and discharge in blue, left axis) and coulombic efficiency (black, right axis) are represented for each current density (A g^{-1}). Each current density is applied for 20 cycles. Dotted lines demark each current density and their corresponding value is indicated above the x-axis.

We monitored for any changes in the molecular conformation of PBDF as a function of doping potential using in situ Raman spectroscopy (Figure S10, Supporting Information).[46] We noticed a progressive decrease in the intensity of the main peak components (aromatic stretching, C—O—C, C=C, and C=O vibrations) with increasing doping potential, echoing the bleaching of these peaks in the FTIR spectra of the charged sample. Moreover, the width of Raman peaks can provide structural information, as it is characteristic of the distribution of molecular orientations in the sample.[47] We noticed a slight broadening of the main peaks with increasing doping potential, indicating a small change in the distribution of the polymer conformations (Figure S10a and Table S4, Supporting Information).[48] Moreover, the Raman spectra of PBDF after 1000 GCD cycles do not display any significant changes compared to the original deposited material, confirming no significant changes in molecular structure after GCD cycling (Figure S10b and Table S5, Supporting Information).

We also aimed to examine morphological characteristics. X-ray diffraction (XRD) spectra of the PBDF thin film (pristine) display multiple peaks, suggesting a relatively ordered microstructure (Figure 2b). As expected, the pristine sample exhibits a (100) peak, associated with a lamellar spacing of 11.10 Å.[24] Ex situ XRD characterization reveals a decrease in intensity and broadening of the (100) peak only upon cycling, with the lamellar spacing decreasing down to 10.20 Å, suggesting decreased order but a generally stable lattice.

In parallel, we monitored for any changes in PBDF electrochemical impedance under GCD cycling to gain insights into changes in the ion transport characteristics by recording the EIS response every 1000 cycles. In the Nyquist plots as a function of GCD cycles (Figure S11, Supporting Information), one observes a progressive decrease of the equivalent series resistance. However, the concomitant decrease of the 45° diffusion slope region indicates less facile mass transport after continuous strain. This is confirmed by the apparent decrease of the dielectric relaxation time constant (τ_0), which demarks the mass transfer-controlled region as the film is cycled, which is further reflected in the decreasing trend of the fitted diffusion time constant τ_D (Figure S11b, c, Supporting Information). On the other hand, the fitted resistance and capacitance (represented by the real part of the capacitance C') remain relatively stable, at 1.68 ± 0.79 Ω and 13.7 ± 4.6 mF, respectively (Figure S11c, Supporting Information). The 3D plot of C' versus frequency and cycle number indicates that PBDF maintains its surface-controlled storage mechanism throughout the GCD cycling (Figure S11d, Supporting Information).

Taken together, the results presented here argue in favor of PBDF as a practical electrode material for electrochemical supercapacitors, leading us to further investigate its use in a more

Table 2. Electrochemical performance of PBDF-based supercapacitor cells measured in degassed 2 M $NaCl_{(aq)}$.

	Voltage window [V]	Energy density [Wh kg^{-1}]	Power density [W kg^{-1}]	Capacitance retention[a)] [%]
PBDF|PBDF	1.0	4.66 ± 0.07	9.02×10^4	80% after 50 000 cycles
PBDF|CPE-K	1.2	5.65 ± 0.01	9.76×10^4	97% after 10 000 cycles
PBDF:rGO|PBDF:rGO	1.0	8.08 ± 0.05	9.18×10^4	16% after 50 000 cycles
PBDF:rGO|CPE-K	1.2	5.63 ± 0.04	9.60×10^4	83% after 100 000 cycles
PBDF|PBDF [1)]	1.0	4.66 ± 0.10	9.97×10^4	50% after 20 000 cycles
PBDF:rGO|CPE-K [1)]	1.2	6.18 ± 0.02	1.10×10^5	78% after 20 000 cycles
PBDF|PBDF [2)]	1.0	4.60 ± 0.12	1.04×10^5	70% after 20 000 cycles
PBDF:rGO|CPE-K [2)]	1.2	6.10 ± 0.03	1.20×10^5	5% after 20 000 cycles

[1)] Swagelok with a (filter paper) separator configuration; [2)] Swagelok without a separator configuration; [a)] Capacitance retention under GCD cycling at 10 A g^{-1}.

practical architecture. We first examined the performance of a symmetric membrane-less (i.e., without a separator) cell — PBDF|PBDF (Figures 2c and S12a–c, Supporting Information). The symmetric cell demonstrates a fill factor (FF) of 81% with a voltage window of 1.0 V, and exhibits rate performances of up to 200 A g^{-1} with 74% capacitance retention, and excellent stability with 100% capacitance retention (comparing at 10 A g^{-1}). The symmetric cell maintains 99.8% Coulombic efficiency throughout all the current densities applied (Figure 2c,d). Furthermore, the PBDF|PBDF cell retains 80% of its capacitance after 50 000 cycles at 10 A g^{-1} (Figure S12c, Supporting Information).

Going one step further, we assembled an asymmetric cell using a p-type conjugated polyelectrolyte, leveraging the synergistic effect of conjugated polymers with complementary electronic transport.[10] We chose the conjugated polyelectrolyte CPE-K as the pairing material, as its stability and rate performance (maintaining 85% of the original capacitance (84 F g^{-1}) at 500 A g^{-1} and 93% capacitance retention after 100 000 cycles at a current density of 35 A g^{-1}) were recently demonstrated in aqueous electrolytes.[26] The asymmetric cell maintains a FF of 89% with an extended voltage window of 1.2 V (Figures 2c and S12e, Supporting Information), and exhibits high-rate operation up to 200 A g^{-1}, maintaining 74% of its initial capacitance with Coulombic efficiency >99% at all rates. For ease of comparison between the different cell configurations reported here, we summarized the relevant cell performance metrics in **Table 2** below. The asymmetric cell also shows reversible operation with 100% capacitance retention when stressed back to a lower load of 10 A g^{-1} (Figure 2e). Additionally, the asymmetric cell displays 97% capacitance retention after 10 000 cycles at a load of 10 A g^{-1} (Figure S12f, Supporting Information).

The average specific capacitance of 202 ± 3 F g^{-1} measured for PBDF represents only 42% of its theoretical capacitance (477 F g^{-1} assuming a 1 electron storage per repeating unit —as calculated above for a 1 V voltage window).[24] We thus sought to explore possible composite formulations to further improve the material utilization efficiency and noted the practice of increasing conductivity via the incorporation of carbon-based materials.[49–52] Therefore, we incorporated either graphene oxide (GO) or reduced graphene oxide (rGO) with PBDF at different weight ratios with the goal of simultaneously improving film conductivity and hydrophilicity. Relevant performance metrics for the different PBDF blends measured in a 3-electrode cell configuration are summarized in Table 1 and **Figure 3a**.

PBDF:rGO (2:1) demonstrated the highest performance, displaying a specific capacitance of 288 ± 8 F g^{-1} and a rate capability up to 270 A g^{-1}. The blend shows high operational reversibility, displaying a 76% capacitance retention at 270 A g^{-1} with a Coulombic efficiency of ≈99% at all rates, and recovered 98% capacitance retention at 10 A g^{-1} after operation at 270 A g^{-1} (Figure S13, Supporting Information). The addition of rGO to PBDF may marginally improve the film conductivity, from 329 ± 132 to 437 ± 36 S cm^{-1} (although we recognize the lack of certainty due to the large error from thickness measurements), without intrinsically modifying the ionic transport, as shown by 4-point probe and EIS (τ_0), respectively (Figure S13d–f, Supporting Information). Raman spectroscopy confirms the incorporation of rGO in the PBDF matrix, evidenced by the presence of the D band at 1347 cm^{-1} and possible G band (≈1583 cm^{-1}) overlapping with the C = C of PBDF at the same wavenumber (Figure S14, Supporting Information).[53,54] From here on, the best-performing blend with a weight ratio of 2:1 PBDF to rGO will be simply referred to as PBDF:rGO.

Using PBDF:rGO, we built symmetric and asymmetric (paired with CPE-K) cells (Figure S18, Supporting Information, and Figure 3b–d). The symmetric PBDF:rGO|PBDF:rGO cell demonstrates good rate capability as it retains 76% capacitance at 200 A g^{-1} and maintains >99% Coulombic efficiency throughout all the current densities tested. The cell recovered 100% capacitance retention at 10 A g^{-1} after operation at 200 A g^{-1} (Figure S18e, Supporting Information). However, the symmetric cell is relatively unstable and can only maintain 16% of its initial capacitance after 50 000 cycles at 10 A g^{-1} (Figure S18f, Supporting Information). On the other hand, the asymmetric PBDF:rGO|CPE-K cell maintains a FF = 88% with an increased voltage window of 1.2 V. Rate performance-wise, the asymmetric supercapacitor exhibits high rate operation up to 200 A g^{-1} with 67% capacitance retention. This asymmetric cell shows high reversibility (100% when cycled back to 10A g^{-1} after 200 A g^{-1}) and exhibits 83% capacitance retention after 100 000 cycles at 10 A g^{-1}, cementing the potential of PBDF-based electrodes for energy storage applications (Figure 3d). Alternatively, when charged to 1.2 V, the asymmetric cell shows relatively slow self-discharge with a behavior comparable to other organic supercapacitor materials, retaining 80% of its voltage after 1 h, and 35% (420 mV)

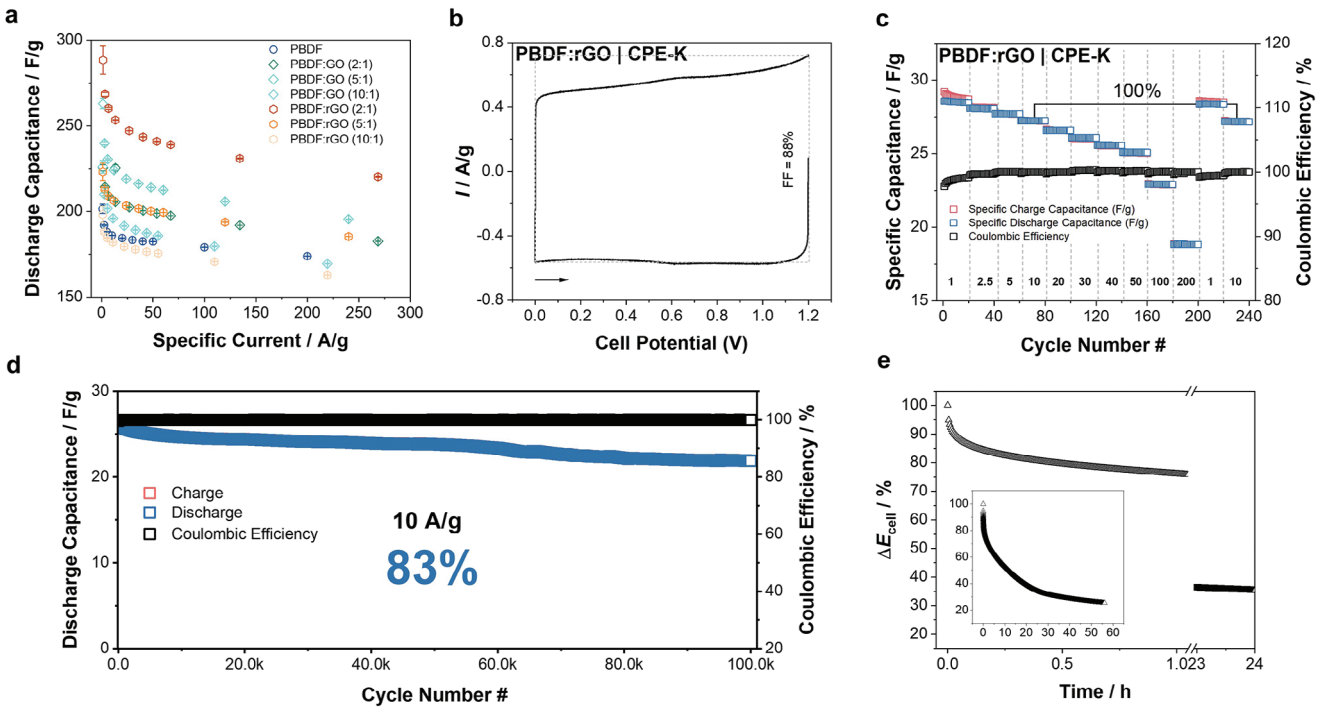

Figure 3. PBDF performance in aqueous supercapacitors. a) Rate performance of PBDF as a function of additives. Error bars represent the standard deviation (N = 10). b) CV curve of the PBDF:rGO|CPE-K supercapacitor in 2 M $NaCl_{(aq)}$. Scan rate is 20 mV s^{-1} and arrow indicates the scan direction. FF = fill factor. c) Rate performance of an asymmetric PBDF:rGO|CPE-K supercapacitor. The specific capacitance (charge in red and discharge in blue, left axis) and coulombic efficiency (black, right axis) are represented for each current density (A g^{-1}). Each current density is applied for 20 cycles. Dotted lines demark each current density and their corresponding value is indicated above the x-axis. The weight ratio of PBDF to rGO is 2:1. d) Cycling stability of PBDF:rGO|CPE-K supercapacitor over 100 000 cycles at a current density of 10 A g^{-1}. The left axis displays the specific capacitance (charge in red and discharge in blue), and the right axis the coulombic efficiency (black). e) Change in PBDF:rGO|CPE-K cell voltage (open circuit) versus time after being charged to 1.2 V at 10 A g^{-1}. Inset represents the change in cell voltage over the total time period investigated.

after 1 day (Figure 3e).[16,55] The main contributors of the potential drop under self-discharge are (i) side Faradaic reactions, (ii) ohmic leakage, and (iii) charge redistribution.[56] In our case, the observed linear dependency of the cell voltage drop on the logarithm of time suggests a Faradaic origin to the first hour of self-discharge (Figure S15, Supporting Information).[57]

A relative comparison of the PDBF supercapacitor cells described here to other polymeric-based reported in the literature is provided in **Figure 4**. Although rGO improves the performance, cells based on PBDF alone are on par or better than most polymeric-based systems, and present the further advantages of neutral and safe aqueous electrolyte and unique composition. On the latter, the solution-processable properties of PBDF, without the need for additional additives, promise scalable fabrication of PBDF-based electrodes.

We also examined the performances of PBDF-based electrodes by using a Swagelok-cell configuration to illustrate their operation in an ideal, realistic configuration, with and without a membrane separator. The advantage of this configuration is the minimized distance (<5 mm in our setup) between the anode and cathode, which reduces the overall resistance of the cell. As shown in Figure 4, all PBDF-based electrodes maintained their performances in both Swagelok configurations, albeit with a decrease in cycling stability (Table 2 and Figure S16, Supporting Information). Another advantage of the Swagelok configuration is the decrease in the cell IR drop, ensuring maximal exploitation of the cell voltage window (Figure S17, Supporting Information). The ability to operate membrane-less cells may prove advantageous for practical implementation by streamlining the overall fabrication process and decreasing the device's weight.

After establishing the performance and stability of PBDF-based supercapacitors, we aimed to demonstrate their applicability to power small electronics. CPE-K was drop cast onto an interdigitated channel to yield an accumulation mode organic electrochemical transistor (OECT) (Figure S18a,b, Supporting Information).[58,59] We connected a PBDF|CPE-K cell, charged to 0.6 V (within 1.8 s), to the Ag/AgCl gate electrode of the OECT, independently biased at a drain voltage of −0.6 V. As the PBDF|CPE-K cell supplies the power to apply a voltage at the gate electrode, the source-drain current of the OECT increased, consistent with the OECT operation. The applied gate voltage is thus modulated by the PBDF|CPE-K cell voltage. Figure S18c, Supporting Information illustrates that PBDF|CPE-K can provide a stable output voltage for more than 10 min, demonstrating the stable operation of small power electronics.

Thereafter, we aim to evaluate PBDF electrochemical performances at higher mass loadings. The PBDF solution concentration was adjusted to yield PBDF thin films with mass loadings of 1 and 2 mg cm^{-2}, an important requirement for practical applications.[27] The CV traces do not show any significant

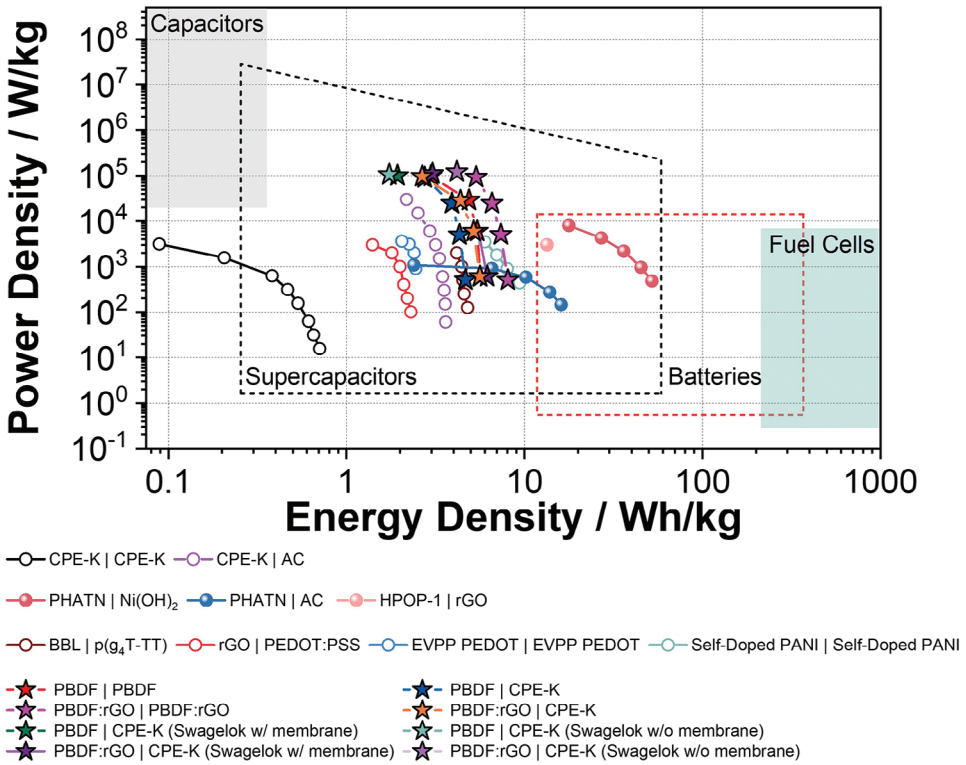

Figure 4. Ragone plot. Power density versus energy density for various PBDF-based supercapacitors and other recently reported organic pseudocapacitor materials. Filled sphere symbols represent 3D-contorted electrode materials. See refs.[16,19,26,41,60–62] for the compared systems. Performances are calculated based on the total active materials weight. PHATN: perylene diimide–hexaazatrinaphthylene; AC: Activated Carbon; HPOP-1: hexaazatrinaphthylene porous organic polymer; BBL: poly(benzimidazobenzophenanthroline); p(g42T-T): poly(2-(3,3′-bis(2-(2-(2-methoxyethoxy)ethoxy)ethoxy)ethoxy)-[2,2′-bithiophen]−5-yl)-thiophene); EVPP-PEDOT: evaporative vapor-phase polymerization PEDOT; PANI: polyaniline.

differences at higher mass loading (Figure S19a, Supporting Information). However, impedance spectra revealed an increased influence of ion diffusion limitation, evidenced by the lengthened Warburg region scaling with mass loading (Figure S19b, Supporting Information). When subjected to GCD cycles, PBDF-based electrodes maintain relatively good performances, showing a specific capacitance of 131 ± 3 F g^{-1} and 120 ± 4 F g^{-1} at 1 and 2 mg cm^{-2} at 1 A g^{-1}, respectively, with Coulombic efficiency >99% at all rates (Figures S19c and S20, Supporting Information). PBDF still demonstrates high-rate capabilities, preserving 78% and 72% of its initial specific capacitance at 50 A g^{-1} when loaded at 1 and 2 mg cm^{-2}, respectively. When subjected to higher current densities, PBDF shows a significant decrease in its specific capacitance at 100 A g^{-1} (63% and 52% retention for 1 and 2 mg cm^{-2}, respectively). The capacitance loss is mainly due to IR drop, becoming more significant at high current densities (Figure S19d, Supporting Information). Furthermore, PBDF stability is maintained at higher mass loadings, showing a >90% capacitance retention after 5000 cycles at 10 A g^{-1} with Coulombic efficiency >99% (Figure S20c, Supporting Information). However, we noted decreased adhesion of the PBDF thin films to the GCE current collector, hampering longer-term characterization. Overall, PBDF demonstrates relevant metric performances as a new n-type conjugated polymer for practical energy storage applications, while further optimization of the cell design and components can further increase the performances. A performance comparison of electrode materials developed for organic supercapacitors can be found in Table S6, Supporting Information.

Last, one of the befitting properties of PBDF is its low-lying LUMO level, with a reduction potential reported at −5.18 eV.[24] This potential provides the material with stability to O_2 and H_2O in its n-doped state. Indeed, Huang. et al. showed that PBDF can retain 95% of its initial conductivity after 35 days of air exposure. Therefore, we sought to investigate if PBDF could retain its performance for energy storage under ambient conditions. Accordingly, we measured the electrochemical performance of PBDF in a three-electrode configuration in ambient 2 M $NaCl_{(aq)}$ and compared it to its demonstrated operation in degassed electrolyte. We note no significant differences in the CV trace, and comparable specific capacitance, rate performance, and cycling stability for the PBDF material (**Figure 5a–c**). We then investigated the influence of oxygen on symmetric (PBDF|PBDF and PBDF:rGO|PBDF:rGO) and asymmetric (PBDF:rGO|CPE-K) configurations. In the symmetric cells, oxygen affects the PBDF:rGO device more than the pristine PBDF one, with the PBDF:rGO cells showing a more pronounced decrease in its rate performance under ambient conditions (Figures 5d and S21,

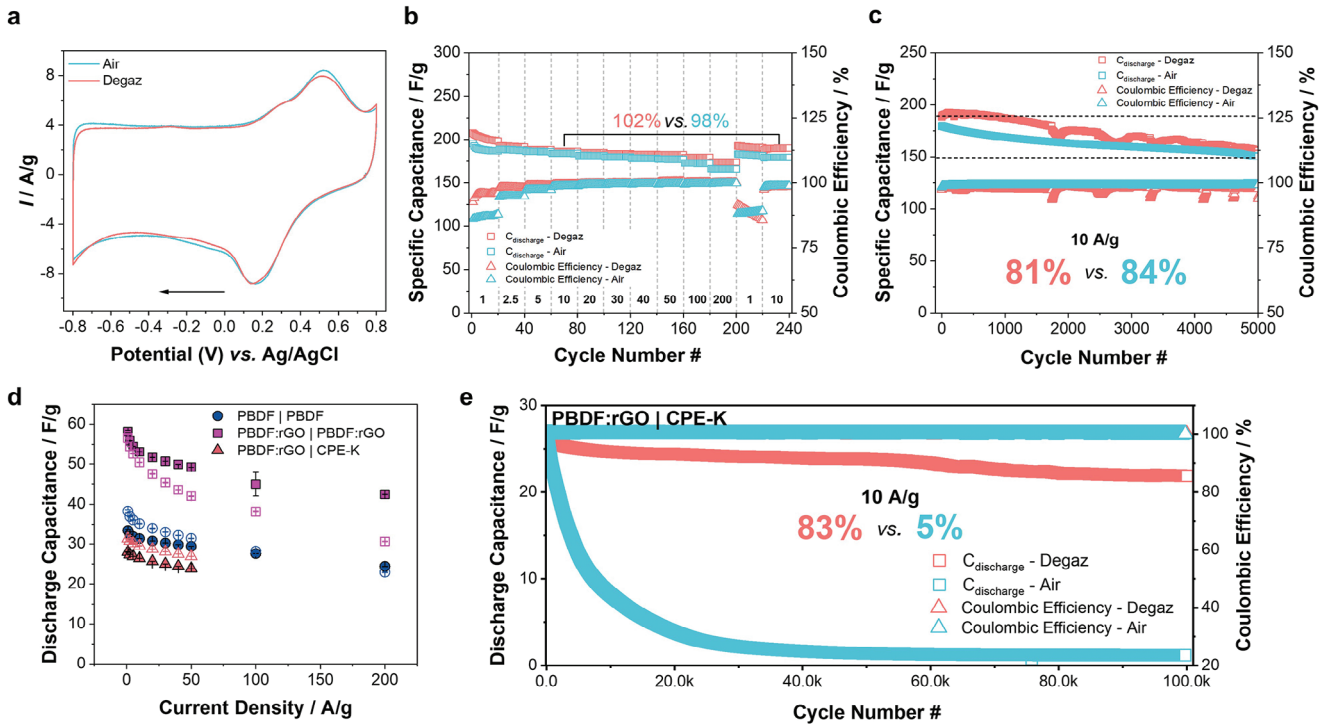

Figure 5. PBDF performance in aqueous supercapacitors under ambient conditions. a) CV curves of PBDF thin film dropcasted on glassy carbon electrode in degassed (red) and ambient (blue) 2 M $NaCl_{(aq)}$ electrolyte. Scan rate is 20 mV s^{-1} and the arrow indicates the scan direction. b) Rate performance of a symmetric PBDF cell in ambient conditions. The specific discharge capacitance (Y-left) and coulombic efficiency (Y-right) degassed (red) and ambient (blue) 2 M $NaCl_{(aq)}$ electrolyte, for each current density (A g^{-1}). Each current density is applied for 20 cycles. Dotted lines demark each current density and their corresponding value is indicated above the x-axis. c) Cycling stability over 5000 cycles at a current density of 10 A g^{-1} in degassed (red) and ambient (blue) 2 M $NaCl_{(aq)}$ electrolyte. d) Rate performance of symmetric PBDF|PBDF, PBDF:rGO|PBDF:rGO, and asymmetric PBDF:rGO|CPE-K supercapacitors in ambient (empty symbols) and degassed (filled symbols) 2 M $NaCl_{(aq)}$ electrolyte. Error bars represent the standard deviation (N = 10). e) Cycling stability of PBDF:rGO|CPE-K supercapacitor in degassed (red) and ambient (blue) 2 M $NaCl_{(aq)}$ electrolyte over 100 000 cycles at a current density of 10 A g^{-1}. The left axis displays the specific discharge capacitance and the right axis the coulombic efficiency. In d and e, the weight ratio of PBDF to rGO is 2:1.

Supporting Information). However, cycling stability appears to be affected by the presence of oxygen, particularly for the asymmetric cell, retaining 50% of its initial capacitance after only 5000 cycles —versus 83% in degassed electrolyte after 100 000 cycles (Figure 5e). We further summarize the performance comparison between degassed and ambient operation for the PBDF-based cells in **Table 3**. Overall, PBDF exhibits stable performance under ambient conditions as a material for energy storage. Furthermore, air operation seems to only affect the whole cell cycling stability, while their capacitance and rate performance are maintained.

3. Conclusion

Motivated by the limited number of n-type conjugated polymers used in energy storage devices and the particularly relevant physical properties of PBDF, we unveiled the potential of this solution-processable, side chain-free, and self-doped n-type conducting polymer as a relevant material for energy storage. Indeed, we show that PBDF-based pseudocapacitive cells boast high specific capacitance and rate capabilities for n-type electrodes, all the while retaining the advantage of a single-component system, thereby simplifying the fabrication process. On that point, the

Table 3. Electrochemical performance of PBDF-based supercapacitor cells measured in 2 M $NaCl_{(aq)}$.

	PBDF|PBDF		PBDF:rGO|PBDF:rGO		PBDF:rGO|CPE-K	
	Degas	Ambient	Degas	Ambient	Degas	Ambient
Energy Density [Wh kg^{-1}]	4.66 ± 0.07	5.34 ± 0.09	8.08 ± 0.05	7.82 ± 0.12	5.63 ± 0.04	6.27 ± 0.01
Power Density [Wh kg^{-1}]	9.02 × 10^4	8.96 × 10^4	9.18 × 10^4	1.17 × 10^5	9.60 × 10^4	9.28 × 10^4
Capacitance retention[a] [%]	80% after 50 000 cycles	50% after 9000 cycles	91% after 20 000 cycles	50% after 6000 cycles	83% after 100 000 cycles	50% after 5000 cycles

[a] Capacitance retention under GCD cycling at 10 A g^{-1}.

preparation of PBDF supercapacitors from DMSO solution argues in favor of ease of application. The facile formation of active layers via drop-casting atop electrode contacts represents a simple and cost-effective fabrication method. A further notable advantage of the approach is the use of DMSO as a solvent for cell fabrication, rendering the process environmentally friendly. The resulting devices operate effectively in an aqueous NaCl electrolyte, making them not only highly efficient but also safe and environmentally sustainable, compared to systems that incorporate highly acidic or concentrated alkaline electrolytes.

We also explored to what extent additives can further improve cell performance, and found that the PBDF:rGO (2:1 weight ratio) blend approaches state-of-the-art performances. When assembled in a symmetric cell or paired with a p-type polyelectrolyte for asymmetric supercapacitor, the PBDF:rGO blend demonstrates power density as high as 10^5 W kg^{-1} and energy density approaching 10 of Wh kg^{-1}. The asymmetric cell demonstrates high-rate operation and sustained performance (83% capacitance retention) over 100 000 cycles. Each configuration showed potentially practical performance for targeted applications. For instance, the symmetric PBDF:rGO|PBDF:rGO cell displays high power density and reversible high-low rate of operation, while its asymmetric configuration using the CPE-K conjugated polyelectrolyte exhibits sustained cycling stability, an important characteristic for wearable or implantable bioelectronics. Furthermore, although sacrificing their cycling stability, air-operable PBDF supercapacitors hold promises for future streamlined and simplified fabrication of high-performance aqueous electrochemical supercapacitors.

Overall, without extensive optimization, PBDF-based supercapacitors not only showcase state-of-the-art characteristics among conjugated polymer-based supercapacitors but also exhibit stability over prolonged cycles, addressing the critical aspects of performance and safety. We envision that further optimization of various parameters (e.g, electrolyte mixture, solid-state electrolytes, alternative additives such as MXenes, and optimized device design) hold the potential to further improve the cell performances and cement PBDF as a competitive material in the practical use of energy storage technologies.

Supporting Information

Supporting Information is available from the Wiley Online Library or from the author.

Acknowledgements

The authors would like to acknowledge the Facility for Analysis, Characterization, Testing and Simulation, the National University of Singapore, and Ms. Tan for her help in acquiring the XRD data. The authors also extend their thanks to Dr.Xinyu Wang for her help in preparing gold-coated substrates. This work was financially supported by the Competitive Research Programme of National Research Foundation Singapore (NRF-CRP27-2021-0004), the Office of Naval Research (ONR-Global, N62909-22-1-2016), and its Research Centre of Excellence award to the Institute for Functional Intelligent Materials (I-FIM, grant EDUNC-33-18-279-V12).

Conflict of Interest

The authors declare no conflict of interest.

Data Availability Statement

The data that support the findings of this study are available in the supplementary material of this article.

Keywords

aqueous super capacitors, conjugated polyelectrolyte, energy storage, n-type conjugated polymer, pseudo capacitors

Received: July 20, 2024
Revised: September 12, 2024
Published online: September 30, 2024

[1] Y. S. Meng, *Chem. Rev.* **2020**, *120*, 6327.
[2] S. Huang, X. Zhu, S. Sarkar, Y. Zhao, *APL Mater.* **2019**, *7*, 100901.
[3] M. I. A. Abdel Maksoud, R. A. Fahim, A. E. Shalan, M. A. Elkodous, S. O. Olojede, A. I. Osman, C. Farrell, A. H. Al-Muhtaseb, A. S. Awed, A. H. Ashour, D. W. Rooney, *Environ. Chem. Lett.* **2021**, *19*, 375.
[4] P. Poizot, J. Gaubicher, S. Renault, L. Dubois, Y. Liang, Y. Yao, *Chem. Rev.* **2020**, *120*, 6490.
[5] S. Fleischmann, J. B. Mitchell, R. Wang, C. Zhan, D.-e. Jiang, V. Presser, V. Augustyn, *Chem. Rev.* **2020**, *120*, 6738.
[6] S. Wustoni, D. Ohayon, A. Hermawan, A. Nuruddin, S. Inal, Y. S. Indartono, B. Yuliarto, *Polym. Rev.* **2023**, *64*, 192.
[7] J. Kim, Y. Kim, J. Yoo, G. Kwon, Y. Ko, K. Kang, *Nat. Rev. Mater.* **2023**, *8*, 54.
[8] S. Biswas, A. Chowdhury, *ChemPhysChem* **2023**, *24*, 202200567.
[9] B. D. Paulsen, K. Tybrandt, E. Stavrinidou, J. Rivnay, *Nat. Mater.* **2020**, *19*, 13.
[10] A. M. Bryan, L. M. Santino, Y. Lu, S. Acharya, J. M. D'Arcy, *Chem. Mater.* **2016**, *28*, 5989.
[11] Q. e. Zhang, A. a. Zhou, J. Wang, J. Wu, H. Bai, *Energy Environ. Sci.* **2017**, *10*, 2372.
[12] R. Boddula, M. F. Ahmer, A. M. Asiri, *Conducting Polymers-Based Energy Storage Materials*, CRC Press, Boca Raton, **2019**.
[13] X. Liu, G. Sun, Y. Gong, C.-F. Liu, S. Wang, S. Xu, X. Yang, L. Yang, W.-Y. Lai, *Sci. China: Chem.* **2022**, *65*, 1767.
[14] R. Di Pietro, D. Fazzi, T. B. Kehoe, H. Sirringhaus, *J. Am. Chem. Soc.* **2012**, *134*, 14877.
[15] D. M. de Leeuw, M. M. J. Simenon, A. R. Brown, R. E. F. Einerhand, *Synth. Met.* **1997**, *87*, 53.
[16] J. C. Russell, V. A. Posey, J. Gray, R. May, D. A. Reed, H. Zhang, L. E. Marbella, M. L. Steigerwald, Y. Yang, X. Roy, C. Nuckolls, S. R. Peurifoy, *Nat. Mater.* **2021**, *20*, 1136.
[17] S. R. Peurifoy, J. C. Russell, T. J. Sisto, Y. Yang, X. Roy, C. Nuckolls, *J. Am. Chem. Soc.* **2018**, *140*, 10960.
[18] L. Jiao, Z. Hu, F. Ma, Y. He, Q. Zhou, L. Xiao, L. Lv, Y. Yang, *J. Energy Storage* **2022**, *52*, 104777.
[19] A. V. Volkov, H. Sun, R. Kroon, T.-P. Ruoko, C. Che, J. Edberg, C. Müller, S. Fabiano, X. Crispin, *ACS Appl. Energy Mater.* **2019**, *2*, 5350.
[20] Y. Zhao, X. Wang, T. Xin, N. Wang, J. Liu, *Sustainable Energy Fuels* **2019**, *3*, 3603.
[21] M. B. Miltenburg, S. Y. An, N. K. Obhi, E. Grignon, B. T. McAllister, D. S. Seferos, *ACS Appl. Polym. Mater.* **2020**, *2*, 5574.
[22] N. Kurra, R. Wang, H. N. Alshareef, *J. Mater. Chem. A* **2015**, *3*, 7368.
[23] W. Xie, T. Li, C. Chen, H. Wu, S. Liang, H. Chang, B. Liu, E. Drioli, Q. Wang, J. C. Crittenden, *Ind. Eng. Chem. Res.* **2019**, *58*, 6413.
[24] H. Tang, Y. Liang, C. Liu, Z. Hu, Y. Deng, H. Guo, Z. Yu, A. Song, H. Zhao, D. Zhao, Y. Zhang, X. Guo, J. Pei, Y. Ma, Y. Cao, F. Huang, *Nature* **2022**, *611*, 271.

[25] Z. Ke, A. Abtahi, J. Hwang, K. Chen, J. Chaudhary, I. Song, K. Perera, L. You, K. N. Baustert, K. R. Graham, J. Mei, *J. Am. Chem. Soc.* **2023**, *145*, 3706.
[26] B. R. P. Yip, R. J. Vázquez, Y. Jiang, S. R. McCuskey, G. Quek, D. Ohayon, X. Wang, G. C. Bazan, *Adv. Mater.* **2023**, *36*, 2308631.
[27] T. S. Mathis, N. Kurra, X. Wang, D. Pinto, P. Simon, Y. Gogotsi, *Adv. Energy Mater.* **2019**, *9*, 1902007.
[28] S. Ardizzone, G. Fregonara, S. Trasatti, *Electrochim. Acta* **1990**, *35*, 263.
[29] D. Baronetto, N. Krstajić, S. Trasatti, H. Vogt, *Electrochim. Acta* **1994**, *39*, 2359.
[30] T. Ma, Y. Yang, D. Johnson, K. Hansen, S. Xiang, R. M. Thakur, A. Djire, J. L. Lutkenhaus, *Joule* **2023**, *7*, 2261.
[31] T. Ma, A. D. Easley, R. M. Thakur, K. T. Mohanty, C. Wang, J. L. Lutkenhaus, *Annu. Rev. Chem. Biomol. Eng.* **2023**, *14*, 187.
[32] J. P. Diard, B. Le Gorrec, C. Montella, *J. Electroanal. Chem.* **1999**, *471*, 126.
[33] J. Diard, B. Le Gorrec, C. Montella, *Handbook of Electrochemical Impedance Spectroscopy-Diffusion Impedances*, Bücher, 30 **2012**.
[34] R. Cabanel, G. Barral, J. P. Diard, B. Le Gorrec, C. Montella, *J. Appl. Electrochem.* **1993**, *23*, 93.
[35] J. Bobacka, A. Lewenstam, A. Ivaska, *J. Electroanal. Chem.* **2000**, *489*, 17.
[36] E. Stavrinidou, P. Leleux, H. Rajaona, M. Fiocchi, S. Sanaur, G. G. Malliaras, *J. Appl. Phys.* **2013**, *113*, 244501.
[37] J. S. Ko, C.-H. Lai, J. W. Long, D. R. Rolison, B. Dunn, J. Nelson Weker, *ACS Appl. Mater. Interfaces* **2020**, *12*, 14071.
[38] N. Kurra, S. Uzun, G. Valurouthu, Y. Gogotsi, *Energy Storage Mater.* **2021**, *39*, 347.
[39] J. S. Ko, M. B. Sassin, J. F. Parker, D. R. Rolison, J. W. Long, *Sustainable Energy Fuels* **2018**, *2*, 626.
[40] D. Pahari, S. G. Puravankara, Safer, *ACS Sustainable Chem. Eng.* **2020**, *8*, 10613.
[41] P. Xu, S. Ouyang, Q. Bai, Q. Ma, Y. Zhu, *J. Polym. Sci.* **2023**, *62*, 1647.
[42] S. K. Pati, D. Patra, S. Muduli, S. Mishra, S. Park, *Small* **2023**, *19*, 2300689.
[43] X.-C. Li, Y. Zhang, C.-Y. Wang, Y. Wan, W.-Y. Lai, H. Pang, W. Huang, *Chem. Sci.* **2017**, *8*, 2959.
[44] Y. Dai, Y. Wang, X. Li, M. Cui, Y. Gao, H. Xu, X. Xu, *Electrochim. Acta* **2022**, *421*, 140470.
[45] B. C. Smith, *Infrared Spectral Interpretation: A Systematic Approach*, CRC press, Boca Raton, **2018**.
[46] P. J. Larkin. In *Infrared and Raman Spectroscopy (Second Edition)*, (Ed: P. J. Larkin), Elsevier, Amsterdam, Netherlands, **2018**.
[47] D. Ohayon, L. Q. Flagg, A. Giugni, S. Wustoni, R. Li, T. C. Hidalgo Castillo, A.-H. Emwas, R. Sheelamanthula, I. McCulloch, L. J. Richter, S. Inal, *ACS Mater Au* **2023**, *3*, 242.
[48] P. Larkin, *Infrared and Raman Spectroscopy: Principles and Spectral Interpretation*, Elsevier, Amsterdam, Netherlands, **2017**.
[49] J. Scotto, G. E. Fenoy, D. Posadas, O. Azzaroni, W. A. Marmisolle. In *Conjugated Polymers for Next-Generation Applications*, (Eds: V. Kumar, K. Sharma, R. Sehgal, S. Kalia), Woodhead Publishing, Sawston, UK, **2022**.
[50] M. Boota, Y. Gogotsi, *Adv. Energy Mater.* **2019**, *9*, 1802917.
[51] J. Ren, X. Zhao, J. Zhang, Qinghua, *Int. J. Electrochem. Sci.* **2016**, *11*, 2550.
[52] C.-M. Chang, C.-J. Weng, C.-M. Chien, T.-L. Chuang, T.-Y. Lee, J.-M. Yeh, Y. Wei, *J. Mater. Chem. A* **2013**, *1*, 14719.
[53] R. Vidano, D. B. Fischbach, *J. Am. Ceram. Soc.* **1978**, *61*, 13.
[54] A. C. Ferrari, *Solid State Commun.* **2007**, *143*, 47.
[55] G. Nikiforidis, S. Wustoni, D. Ohayon, V. Druet, S. Inal, *ACS Appl. Energy Mater.* **2020**, *3*, 7896.
[56] B. E. Conway, W. G. Pell, T. C. Liu, *J. Power Sources* **1997**, *65*, 53.
[57] B. E. Conway, *Electrochemical Supercapacitors: Scientific Fundamentals and Technological Applications*, Springer Science & Business Media, Berlin, **2013**.
[58] J. Song, F. Yan, *IEEE J. Flex. Electron.* **2022**, *1*, 88.
[59] D. Ohayon, V. Druet, S. Inal, *Chem. Soc. Rev.* **2023**, *52*, 1001.
[60] J. M. D'Arcy, M. F. El-Kady, P. P. Khine, L. Zhang, S. H. Lee, N. R. Davis, D. S. Liu, M. T. Yeung, S. Y. Kim, C. L. Turner, A. T. Lech, P. T. Hammond, R. B. Kaner, *ACS Nano* **2014**, *8*, 1500.
[61] Y. Liu, B. Weng, J. M. Razal, Q. Xu, C. Zhao, Y. Hou, S. Seyedin, R. Jalili, G. G. Wallace, J. Chen, *Sci. Rep.* **2015**, *5*, 17045.
[62] H. R. Ghenaatian, M. F. Mousavi, S. H. Kazemi, M. Shamsipur, *Synth. Met.* **2009**, *159*, 1717.